

The selection rule of graphene in a composite magnetic field

Y. C. Ou,¹ Y. H. Chiu,^{2,4} P. H. Yang,^{3,5} and M. F. Lin^{1,*}

¹*Department of Physics, National Cheng Kung University, Tainan, Taiwan*

²*National Center for Theoretical Sciences, National Tsing Hua University, Hsinchu, Taiwan*

³*National Center for High-Performance Computing (South), Tainan, Taiwan*

⁴airegg.py90g@nctu.edu.tw

⁵yangp@nchc.narl.org.tw

^{*}mflin@mail.ncku.edu.tw

Abstract: The generalized tight-binding model with exact diagonalization method is developed to calculate the optical properties of monolayer graphene in the presence of composite magnetic fields. The ratio of the uniform magnetic field and the modulated one accounts for a strong influence on the structure, number, intensity and frequency of absorption peaks, and thus the extra selection rules that are subsequently induced can be explained. When the modulated field increases, each symmetric peak, under a uniform magnetic field, splits into a pair of asymmetric peaks with lower intensities. The threshold absorption frequency exhibits an obvious evolution in terms of a redshift. These absorption peaks obey the same selection rule that is followed by Landau level transitions. Moreover, at a sufficiently strong modulation strength, the extra peaks in the absorption spectrum might arise from different selection rules.

© 2014 Optical Society of America

OCIS codes: (160.4760) Optical properties; (300.1030) Absorption; (300.6170) Spectra; (310.6860) Thin films, optical properties.

References and links

1. K. S. Novoselov, A. K. Geim, S. V. Morozov, D. Jiang, Y. Zhang, and S. V. Dubonos, "Electric Field Effect in Atomically Thin Carbon Films," *Science* **306**, 666–669 (2004).
2. K. S. Novoselov, A. K. Geim, S. V. Morozov, D. Jiang, M. I. Katsnelson, I. V. Grigorieva, S. V. Dubonos, and A. A. Firsov, "Two-dimensional gas of massless Dirac fermions in graphene," *Nature (London)* **438**, 197–200 (2005).
3. J. Coraux, A. T. N'Diaye, C. Busse, and T. Michely, "Structural Coherency of Graphene on Ir(111)," *Nano Lett.* **8**, 565–570 (2008).
4. N. W. Nicholas, L. M. Connors, F. Ding, B. I. Yakobson, H. K. Schmidt, and R. H. Hauge, "Templated growth of graphenic materials," *Nanotechnology* **20**, 245607 (2009).
5. C. Berger, Z. Song, X. Li, X. Wu, N. Brown, C. Naud, D. Mayou, T. Li, J. Hass, A. N. Marchenkov, E. H. Conrad, P. N. First, and W. A. de Heer, "Electronic Confinement and Coherence in Patterned Epitaxial Graphene," *Science* **312**, 1191–1196 (2006).
6. J. Campos-Delgado, Y. A. Kim, T. Hayashi, A. Morelos-Gómez, M. Hofmann, H. Muramatsu, M. Endo, H. Terrones, R. D. Shull, M. S. Dresselhaus, and M. Terrones, "Thermal stability studies of CVD-grown graphene nanoribbons: Defect annealing and loop formation," *Chem. Phys. Lett.* **469**, 177–182 (2009).
7. J. Campos-Delgado, J. M. Romo-Herrera, X. Jia, D. A. Cullen, H. Muramatsu, Y. A. Kim, T. Hayashi, Z. Ren, D. J. Smith, Y. Okuno, T. Ohba, H. Kanoh, K. Kaneko, M. Endo, H. Terrones, M. S. Dresselhaus, and M. Terrones, "Bulk Production of a New Form of sp² Carbon: Crystalline Graphene Nanoribbons," *Nano Lett.* **8**, 2773–2778 (2008).

8. J. H. Ho, Y. H. Lai, Y. H. Chiu, and M. F. Lin, "Landau levels in graphene," *Physica E* **40**, 1722–1725 (2008).
9. F. D. M. Haldane, "Model for a Quantum Hall Effect without Landau Levels: Condensed-Matter Realization of the "Parity Anomaly"," *Phys. Rev. Lett.* **61**, 2015 (1988).
10. Z. Jiang, E. A. Henriksen, L. C. Tung, Y. J. Wang, M. E. Schwartz, M. Y. Hun, P. Kim, and H. L. Stormer, "Infrared Spectroscopy of Landau Levels of Graphene," *Phys. Rev. Lett.* **98**, 197403 (2007).
11. Y. Zhang, Y. W. Tan, H. L. Stormer, and P. Kim, "Experimental observation of the quantum Hall effect and Berry's phase in graphene," *Nature* **438**, 201–204 (2005).
12. P. R. Wallace, "The Band Theory of Graphite," *Phys. Rev.* **71**, 622 (1947).
13. M. I. Katsnelson, K. S. Novoselov, and A. K. Geim, "Chiral tunnelling and the Klein paradox in graphene," *Nat. Phys.* **2**, 620–625 (2006).
14. K. I. Bolotin, F. Ghahari, M. D. Shulman, H. L. Stormer, and P. Kim, "Observation of the fractional quantum Hall effect in graphene," *Nature* **462**, 196–199 (2009).
15. K. S. Novoselov, Z. Jiang, Y. Zhang, S. V. Morozov, H. L. Stormer, U. Zeitler, J. C. Maan, G. S. Boebinger, P. Kim, and A. K. Geim, "Room-Temperature Quantum Hall Effect in Graphene," *Science* **315**, 1379 (2007).
16. R. S. Deacon, K. C. Chuang, R. J. Nicholas, K. S. Novoselov, and A. K. Geim, "Cyclotron resonance study of the electron and hole velocity in graphene monolayers," *Phys. Rev. B* **76**, 081406 (2007).
17. S. Yuan, R. Roldán, and M. I. Katsnelson, "Polarization of graphene in a strong magnetic field beyond the Dirac cone approximation," *Solid State Commun.* **152**, 1446–1455 (2012).
18. R. R. Hartmann, N. J. Robinson, and M. E. Portnoi, "Smooth electron waveguides in graphene," *Phys. Rev. B* **81**, 245431 (2010).
19. D. A. Stone, C. A. Downing, and M. E. Portnoi, "Searching for confined modes in graphene channels: The variable phase method," *Phys. Rev. B* **86**, 075464 (2012).
20. M. Ramezani Masir, P. Vasilopoulos and F. M. Peeters, "Magnetic Kronig–Penney model for Dirac electrons in single-layer graphene," *New J. Phys.* **11**, 095009 (2009).
21. H. C. Kao, M. Lewkowicz, Y. Korniyenko, B. Rosenstein, "Dynamical approach to ballistic transport in graphene," *Comput. Phys. Commun.* **182**, 112–114 (2011).
22. D. P. Arovas, L. Brey, H. A. Fertig, E.-A. Kim, and K. Ziegler, "Dirac spectrum in piecewise constant one-dimensional (1D) potentials," *New J. Phys.* **12**, 123020 (2010).
23. C. Bai and X. Zhang, "Klein paradox and resonant tunneling in a graphene superlattice," *Phys. Rev. B* **76**, 075430 (2007).
24. M. Barbier, F. M. Peeters, P. Vasilopoulos, and J. M. Pereira, "Dirac and Klein-Gordon particles in one-dimensional periodic potentials," *Phys. Rev. B* **77**, 115446 (2008).
25. L. Brey and H. A. Fertig, "Emerging Zero Modes for Graphene in a Periodic Potential," *Phys. Rev. Lett.* **103**, 046809 (2009).
26. M. Barbier, P. Vasilopoulos, and F. M. Peeters, "Extra Dirac points in the energy spectrum for superlattices on single-layer graphene," *Phys. Rev. B* **81**, 075438 (2010).
27. L.-G. Wang and S.-Y. Zhu, "Electronic band gaps and transport properties in graphene superlattices with one-dimensional periodic potentials of square barriers," *Phys. Rev. B* **81**, 205444 (2010).
28. V. P. Gusynin and S. G. Sharapov, "Magnetic oscillations in planar systems with the Dirac-like spectrum of quasiparticle excitations. II. Transport properties," *Phys. Rev. B* **71**, 125124 (2005).
29. M. S. Purewal, Y. Zhang, and P. Kim, "Unusual transport properties in carbon based nanoscaled materials: nanotubes and graphene," *Phys. Status Solidi B* **243**, 3418–3422 (2006).
30. S. K. Firoz Islam, N. K. Singh and T. K. Ghosh, "Thermodynamic properties of a magnetically modulated graphene monolayer," *J. Phys.: Condens. Matter* **23**, 445502 (2011).
31. M. Tahir, K. Sabeeh and A. MacKinnon, "Temperature effects on the magnetoplasmon spectrum of a weakly modulated graphene monolayer," *J. Phys.: Condens. Matter* **23**, 425304 (2011).
32. M. Tahir, K. Sabeeh and A. MacKinnon, "Weiss oscillations in the electronic structure of modulated graphene," *J. Phys.: Condens. Matter* **19**, 406226 (2007).
33. M. Tahir and K. Sabeeh, "Theory of Weiss oscillations in the magnetoplasmon spectrum of Dirac electrons in graphene," *Phys. Rev. B* **76**, 195416 (2007).
34. A. Matulis and F. M. Peeters, "Appearance of enhanced Weiss oscillations in graphene: Theory," *Phys. Rev. B* **75**, 125429 (2007).
35. Y. C. Ou, J. K. Sheu, Y. H. Chiu, R. B. Chen, and M. F. Lin, "Influence of modulated fields on the Landau level properties of graphene," *Phys. Rev. B* **83**, 195405 (2011).
36. Y. C. Ou, Y. H. Chiu, J. M. Lu, W. P. Su, and M. F. Lin, "Electric modulation effect on magneto-optical spectrum of monolayer graphene," *Comput. Phys. Commun.* **184**, 1821–1826 (2013).
37. C. P. Chang, C. L. Lu, F. L. Shyu, R. B. Chen, Y. K. Fang, and M. F. Lin, "Magnetoelectronic properties of a graphite sheet," *Carbon* **42**, 2975–2980 (2004).
38. P. Plochocka, C. Faugeras, M. Orlita, M. L. Sadowski, G. Martinez, M. Potemski, M. O. Goerbig, J.-N. Fuchs, C. Berger, and W. A. de Heer, "High-Energy Limit of Massless Dirac Fermions in Multilayer Graphene using Magneto-Optical Transmission Spectroscopy," *Phys. Rev. Lett.* **100**, 087401 (2008).
39. Y. H. Chiu, J. H. Ho, C. P. Chang, D. S. Chuu, and M. F. Lin, "Low-frequency magneto-optical excitations of

- a graphene monolayer: Peierls tight-binding model and gradient approximation calculation," *Phys. Rev. B* **78**, 245411 (2008).
40. Y. H. Chiu, Y. C. Ou, Y. Y. Liao, and M. F. Lin, "Optical-absorption spectra of single-layer graphene in a periodic magnetic field," *J. Vac. Sci. Technol. B* **28**, 386–390 (1992).
 41. Y. H. Chiu, Y. H. Lai, J. H. Ho, D. S. Chu, and M. F. Lin, "Electronic structure of a two-dimensional graphene monolayer in a spatially modulated magnetic field: Peierls tight-binding model," *Phys. Rev. B* **77**, 045407 (2008).
 42. Y. H. Lai, J. H. Ho, C. P. Chang, and M. F. Lin, "Magnetoelectronic properties of bilayer Bernal graphene," *Phys. Rev. B* **77**, 085426 (2008).
 43. J. H. Ho, Y. H. Chiu, S. J. Tsai, and M. F. Lin, "Semimetallic graphene in a modulated electric potential," *Phys. Rev. B* **79**, 115427 (2009).
 44. J. H. Ho, Y. H. Lai, Y. H. Chiu, and M. F. Lin, "Modulation effects on Landau levels in a monolayer graphene," *Nanotechnology* **19**, 035712 (2008).
 45. N. Nemec and G. Cuniberti, "Hofstadter butterflies of bilayer graphene," *Phys. Rev. B* **75**, 201404 (2007).
 46. T. G. Pedersen, "Tight-binding theory of Faraday rotation in graphite," *Phys. Rev. B* **68**, 245104 (2003).
 47. G. Dresselhaus and M. S. Dresselhaus, "Fourier Expansion for the Electronic Energy Bands in Silicon and Germanium," *Phys. Rev.* **160**, 649–679 (1967).
 48. L. G. Johnson and G. Dresselhaus, "Optical Properties of Graphite," *Phys. Rev. B* **7**, 2275–2285 (1973).
 49. N. V. Smith, "Photoemission spectra and band structures of d-band metals. VII. Extensions of the combined interpolation scheme," *Phys. Rev. B* **19**, 5019–5027 (1979).
 50. L. C. Lew Yan Voon and L. R. Ram-Mohan, "Tight-binding representation of the optical matrix elements: Theory and applications," *Phys. Rev. B* **47**, 15500–15508 (1993).
 51. J. Blinowski, N. H. Hau, C. Rigaux, J. P. Vieren, R. L. Toullee, G. Furdin, A. Herold, and J. Melin, "Band structure model and dynamical dielectric function in lowest stages of graphite acceptor compounds," *J. Phys. (Paris)* **41**, 47–58 (1980).
 52. M. F. Lin and Kenneth W.-K. Shung, "Plasmons and optical properties of carbon nanotubes," *Phys. Rev. B* **50**, 17744–17747 (1994).
 53. Y. H. Ho, Y. H. Chiu, D. H. Lin, C. P. Chang, and M. F. Lin, "Magneto-optical Selection Rules in Bilayer Bernal Graphene," *ACS Nano* **4**, 1465–1472 (2010).
 54. M. Kato, A. Endo, S. Katsumoto, and Y. Iye, "Two-dimensional electron gas under a spatially modulated magnetic field: A test ground for electron-electron scattering in a controlled environment," *Phys. Rev. B* **58**, 4876–4881 (1998).
 55. Y. H. Ho, J. Y. Wu, R. B. Chen, Y. H. Chiu, and M. F. Lin, "Optical transitions between Landau levels: AA-stacked bilayer graphene," *Appl. Phys. Lett.* **97**, 101905 (2010).
 56. Y. Zheng and T. Ando, "Hall conductivity of a two-dimensional graphite system," *Phys. Rev. B* **65**, 245420 (2002).
 57. Y. C. Chuang, J. Y. Wu, and M. F. Lin, "Electric Field Dependence of Excitation Spectra in AB-Stacked Bilayer Graphene," *Sci. Rep.* **3**, 1368 (2013).
 58. C. W. Chiu, Y. C. Huang, F. L. Shyu, and M. F. Lin, "Optical absorption spectra in ABC-stacked graphene superlattice," *Synth. Met.* **162**, 800–804 (2012).
 59. S. Yuan, R. Roldán, and M. I. Katsnelson, "Landau level spectrum of ABA- and ABC-stacked trilayer graphene," *Phys. Rev. B* **84**, 125455 (2011).
 60. R. B. Chen, Y. H. Chiu, and M. F. Lin, "A theoretical evaluation of the magneto-optical properties of AA-stacked graphite," *Carbon* **54**, 268–276 (2012).
 61. X.-F. Wang and T. Chakraborty, "Coulomb screening and collective excitations in a graphene bilayer," *Phys. Rev. B* **75**, 041404 (2007).
 62. X.-F. Wang and T. Chakraborty, "Collective excitations of Dirac electrons in a graphene layer with spin-orbit interactions," *Phys. Rev. B* **75**, 033408 (2007).
 63. N. M. R. Peres, F. Guinea, and A. H. Castro Neto, "Coulomb interactions and ferromagnetism in pure and doped graphene," *Phys. Rev. B* **72**, 174406 (2005).
 64. J. Y. Wu, S. C. Chen, Oleksiy Roslyak, Godfrey Gumbs, M. F. Lin, "Plasma Excitations in Graphene: Their Spectral Intensity and Temperature Dependence in Magnetic Field," *ACS Nano* **5**, 1026–1032 (2011).
 65. A. Iyengar, Jianhui Wang, H. A. Fertig, and L. Brey, "Excitations from filled Landau levels in graphene," *Phys. Rev. B* **75**, 125430 (2007).
 66. R. Roldán, J. N. Fuchs, and M. O. Goerbig, "Spin-flip excitations, spin waves, and magnetoexcitons in graphene Landau levels at integer filling factors," *Phys. Rev. B* **82**, 205418 (2010).
 67. V. P. Gusynin and S. G. Sharapov, "Transport of Dirac quasiparticles in graphene: Hall and optical conductivities," *Phys. Rev. B* **73**, 245411 (2006).
 68. V. P. Gusynin, V. A. Miransky, S. G. Sharapov, and I. A. Shovkovy, "Excitonic gap, phase transition, and quantum Hall effect in graphene," *Phys. Rev. B* **74**, 195429 (2006).
 69. M. Koshino and T. Ando, "Transport in bilayer graphene: Calculations within a self-consistent Born approximation," *Phys. Rev. B* **73**, 245403 (2006).
 70. J. Nilsson, A. H. Castro Neto, F. Guinea, and N. M. R. Peres, "Electronic Properties of Graphene Multilayers,"

1. Introduction

Monolayer graphene (MG), constructed from a single layer of carbon atoms densely packed in a hexagonal lattice, was successfully produced by mechanical exfoliation [1, 2] and chemical vapor deposition [3-7]. This particular material constitutes an excellent system for studying two-dimensional (2D) physical properties, e.g., quantum Hall effects [8-11]. In the low-energy region $|E^{c,v}| \leq 1$ eV, MG possesses isotropic linear bands crossing at the \mathbf{K} (\mathbf{K}') point and is regarded as a 2D zero-gap semiconductor, where c (v) indicates the conduction (valence) bands [12]. The linear bands are symmetric about the Fermi level ($E_F = 0$) and become nonlinear and anisotropic at higher energy $|E^{c,v}| > 1$ [12]. Most importantly, the quasiparticles related to the linear bands can be described by the Dirac-like Hamiltonian [13] that is associated with relativistic particles and dominates the low-energy physical properties [11, 14, 15]. This special electronic structure has been verified by experimental measurements [2, 16].

MG has become a potential material candidate for nano-devices due to its exotic electronic properties. A good understanding of the behavior of MG under external fields [17-27] is useful for improving the characteristics of graphene-based nano-devices. In the presence of a uniform perpendicular magnetic field, the linear bands change into dispersionless Landau levels (LLs) which obey the specific relationship $E^{c,v} \propto \sqrt{n^{c,v}} B_0$, where n^c (n^v) is the quantum number of the conduction (valence) states and B_0 is the magnetic field strength. The related anomalous quantum Hall effects [11, 28, 29] and particular optical excitations [17] have been verified experimentally [10, 11]. The anisotropic behavior of dispersive quasi-Landau levels (QLLs) and the special selection rules presented in the related optical absorption spectra are shown for a modulated magnetic field. Furthermore, Haldane predicted the existence of quantum Hall effects in MG when it is subjected to the modulated magnetic field even without any net magnetic flux through the entire space [9]. For two cases of composite fields, a uniform magnetic field combined with a modulated magnetic field and a uniform magnetic field combined with a modulated electric potential, the LL properties are drastically changed by the modulated field [30-34]. The broken symmetry, displacement of the localization center, and alteration of the amplitude of the LL wave functions can, in some cases, be observed [35, 36].

MG is predicted to exhibit feature-rich optical absorption spectra. The spectral intensity is proportional to the frequency, but no prominent peak exists at low frequency [37]. However, a uniform perpendicular magnetic field can lead to a number of symmetric absorption peaks originating from LLs. Each peak obeys the specific selection rule $\Delta n = |n^c - n^v| = 1$, which has been confirmed by magneto-transmission measurements [16, 17, 38]. The selection rule is ascribed to the spatial symmetric configuration of the magneto-electronic wave function. Under a modulated magnetic field, the optical spectra exhibit many asymmetric principal peaks and subpeaks. The former satisfy a selection rule similar to those pertinent to LLs, while the latter do not [39, 40]. For a better understanding, it is necessary to investigate the primary features of optical excitations in composite magnetic fields with various field strength ratios between the uniform and the modulated fields.

The generalized tight-binding model with exact diagonalization method is developed to resolve the optical absorption spectra. By rearranging the tight-binding functions, the giant Hermitian matrix corresponding to the experimental fields can be transformed into a band-like matrix, so that the numerical computation time is greatly reduced [41-44]. Moreover, the π -electronic structure of MG can be solved in the wide energy range of 5 eV, a solution proven valid regardless of whether a magnetic, electric or composite field is applied. In this work, we

focus on the optical absorption spectra of MG under a composite magnetic field. By means of controlling the ratio between a uniform magnetic field and a modulated one, the magneto-optical properties can be thoroughly explored and then presented in detail. For an increased modulated field, each symmetric peak, under a uniform magnetic field, splits into a pair of asymmetric peaks. Redshift is an obvious evolution exhibited by the threshold absorption frequency. Perceivably, each peak obeys the same selection rule as in the situation where only the uniform magnetic field exists until the modulated field is increased beyond a certain point. As a result, important differences of the absorption peaks are observed with regard to their structure, number, intensity, frequency and selection rule when the applied magnetic field is varied among the uniform, composite and purely modulated ones.

2. Band-like Hamiltonian matrix in external fields

The low-frequency optical properties of MG are determined by the π -electronic structure resulting from the $2p_z$ orbitals of the carbon atoms. The generalized tight-binding model with the exact diagonalization method is developed to characterize the electronic properties, and then the gradient approximation is applied to obtain the optical-absorption spectra. In the presence of magnetic fields, the vector potential induces Peierls phases [39, 41, 45, 46], which are then accumulated in the Bloch wave functions. Such a phase owns the extra period R or changes the unit cell. The enlarged rectangular unit cell, marked by the green rectangle in Fig. 1, is chosen as the primitive unit cell. In this work, the major discussions focus on R along the armchair direction. MG is subjected to three kinds of magnetic fields: a uniform perpendicular magnetic field, a periodically modulated magnetic field, and a composite magnetic field comprised of both the uniform and modulated parts. In the case of the uniform magnetic field $\mathbf{B}_0 = B_0 \hat{z}$, the period is given by $R = R_0 = \phi_0 / (3\sqrt{3}b'^2 B_0 / 2)$, where $b' = 1.42 \text{ \AA}$ is the C-C bond length, and $\phi_0 (= hc/e = 4.1356 \times 10^{-15} \text{ [T/m}^2])$ is the unit flux quantum. In the case of the modulated magnetic field, $\mathbf{B}_M = B_M \sin(2\pi x/l_M) \hat{z}$ is exerted along the armchair direction, where B_M is the field strength and l_M is the period length with the modulation period $R = R_M = l_M / 3b'$. In the case of the composite field, the period $R = R_C$ is the least common multiple of R_0 and R_M . An enlarged rectangular unit cell induced by an external field encompasses $2R$ a atoms and $2R$ b atoms. The Hamiltonian matrix is a $4R \times 4R$ Hermitian matrix spanned by $4R$ TB functions. Based on the arrangement of odd and even atoms in the primitive cell, the Bloch wave function $|\Psi_{\mathbf{k}}\rangle$ can be expressed as:

$$|\Psi_{\mathbf{k}}\rangle = \sum_{m=1}^{2R-1} (A_{\mathbf{o}}^{c,v} |a_{m\mathbf{k}}\rangle + B_{\mathbf{o}}^{c,v} |b_{m\mathbf{k}}\rangle) + \sum_{m=2}^{2R} (A_{\mathbf{e}}^{c,v} |a_{m\mathbf{k}}\rangle + B_{\mathbf{e}}^{c,v} |b_{m\mathbf{k}}\rangle), \quad (1)$$

where $|a_{m\mathbf{k}}\rangle$ ($|b_{m\mathbf{k}}\rangle$) is the TB function corresponding to the $2p_z$ orbital of the m th a (b) atom. $A_{\mathbf{o}}^{c,v}$ ($A_{\mathbf{e}}^{c,v}$) and $B_{\mathbf{o}}^{c,v}$ ($B_{\mathbf{e}}^{c,v}$) are the subenvelope functions representing the amplitudes of the wave functions of the a - and b -atoms respectively, where o (e) represents an odd (even) integer. Since the features of $A_{\mathbf{o}}^{c,v}$ ($B_{\mathbf{o}}^{c,v}$) and $A_{\mathbf{e}}^{c,v}$ ($B_{\mathbf{e}}^{c,v}$) are similar, choosing only the amplitudes $A_{\mathbf{o}}^{c,v}$ and $B_{\mathbf{o}}^{c,v}$ suffices to understand the electronic and optical properties. The $4R \times 4R$ Hamiltonian matrix, which determines the magneto-electronic properties, is a giant Hermitian matrix with respect to the external fields actually used in the experiments. To make the calculations more efficient, the matrix is transformed into an $M \times 4R$ band-like matrix by a suitable rearrangement of the tight-binding functions, where M is much smaller than $4R$. For example, one can arrange the basis functions according to the following sequence $|a_{1\mathbf{k}}\rangle, |b_{2R\mathbf{k}}\rangle, |b_{1\mathbf{k}}\rangle, |a_{2R\mathbf{k}}\rangle, |a_{2\mathbf{k}}\rangle, |b_{2R-1\mathbf{k}}\rangle, |b_{2\mathbf{k}}\rangle, |a_{2R-1\mathbf{k}}\rangle, \dots, |a_{R-1\mathbf{k}}\rangle, |b_{R+2\mathbf{k}}\rangle, |b_{R-1\mathbf{k}}\rangle, |a_{R+2\mathbf{k}}\rangle, |a_{R\mathbf{k}}\rangle, |b_{R+1\mathbf{k}}\rangle, |b_{R\mathbf{k}}\rangle, |a_{R+1\mathbf{k}}\rangle$. By performing these calculations, the nonzero Hamiltonian matrix elements can be formulated as

$$\langle b_{m'\mathbf{k}} | H | a_{m\mathbf{k}} \rangle = [t_{1k}(m) + t_{2k}(m)] \delta_{m',m} + t_{3k}(m) \delta_{m',m-1}, \quad (2)$$

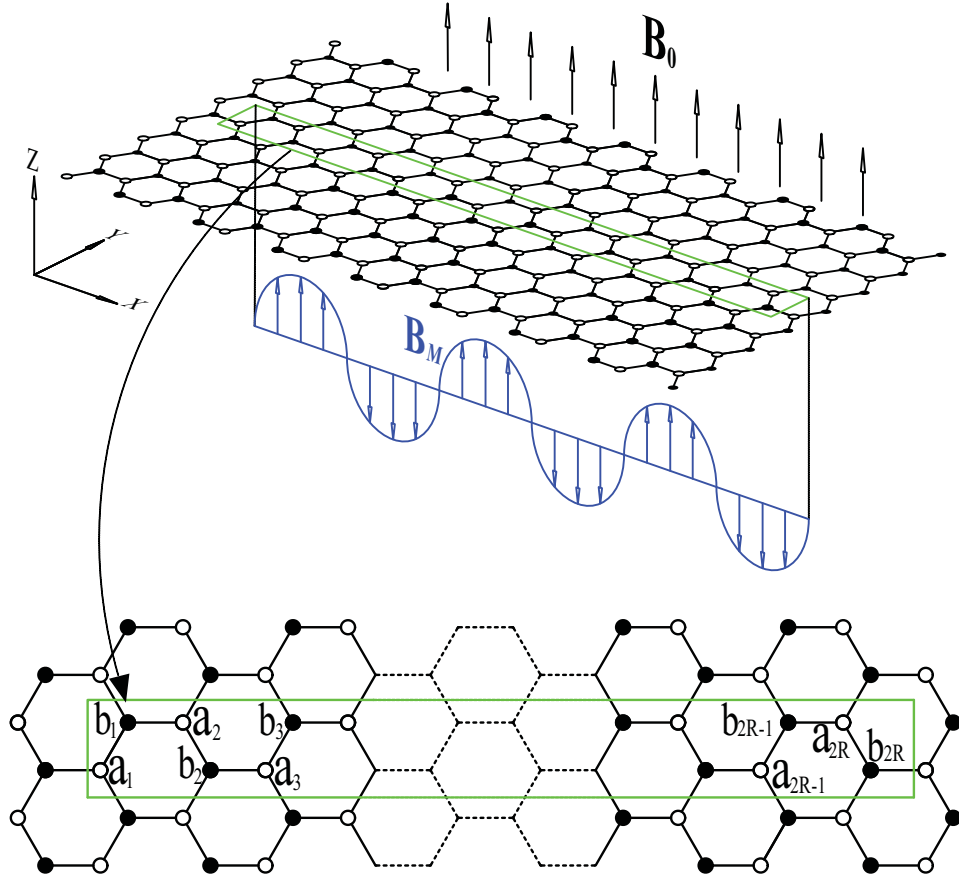


Fig. 1. The primitive cell of a monolayer graphene in a uniform magnetic field and a spatially modulated magnetic field along the armchair direction.

where $t_{1k}(m) = \gamma_0 \exp[i(k_x b'/2 + k_y \sqrt{3}b'/2 - G_0 - G_M)]$, $t_{2k}(m) = \gamma_0 \exp[i(k_x b'/2 - k_y \sqrt{3}b'/2 - G_0 - G_M)]$ and $t_{3k}(m) = \gamma_0 \exp[-i(k_x b')]$ are the three nearest-neighbor hopping integrals. $\gamma_0 = 2.5$ eV is the nearest-neighbor interaction. $G_0 = -\frac{\pi(m-1)+1/6}{R_0}$ and $G_M = \frac{6(R_M)^2}{\pi} \frac{\phi'}{\phi_0} \cos[\frac{\pi}{R_M}(m - \frac{5}{6})] \sin(\frac{\pi}{6R_M})$ are the Peierls phases in the off-diagonal elements associated with the uniform and modulated magnetic fields, respectively.

When electrons are excited from occupied valence to unoccupied conduction bands by an electro-magnetic field, only inter- π -band excitations exist in the zero temperature case. Based on Fermi's golden rule, the optical absorption function results in the following form

$$A(\omega) \propto \sum_{c,v,\tilde{n},\tilde{n}'} \int_{1stBZ} \frac{d\mathbf{k}}{(2\pi)^2} \left| \langle \Psi^c(\mathbf{k}, n) | \frac{\hat{\mathbf{E}} \cdot \mathbf{P}}{m_e} | \Psi^v(\mathbf{k}, n') \rangle \right|^2 \times \text{Im} \left[\frac{f(E^c(\mathbf{k}, n)) - f(E^v(\mathbf{k}, n'))}{E^c(\mathbf{k}, n) - E^v(\mathbf{k}, n') - \omega - i\Gamma} \right], \quad (3)$$

where $f(E(\mathbf{k}, \tilde{n}))$ is the Fermi-Dirac distribution function, $\Gamma (= 2 \times 10^{-4} \gamma_0)$ is the broadening parameter, \mathbf{P} is the momentum, and m_e is the bare electron mass. Meanwhile, n and n' are the quantum numbers with respect to the initial and final states. The electric polarization $\hat{\mathbf{E}}$ along \hat{y} is taken into account for discussions. Within the gradient approximation [47-51], the velocity matrix element $M^{cv} = \langle \Psi^c(\mathbf{k}, n) | \frac{\hat{\mathbf{E}} \cdot \mathbf{P}}{m_e} | \Psi^v(\mathbf{k}, n') \rangle$ is formulated as

$$\sum_{m,m'=1}^{2R_C} [(A_{\mathbf{o}}^c + A_{\mathbf{e}}^c)^* \times (B_{\mathbf{o}}^v + B_{\mathbf{e}}^v)] \nabla_{\mathbf{k}} \langle a_{m\mathbf{k}} | H | b_{m'\mathbf{k}} \rangle + h.c.. \quad (4)$$

Equation (4) implies that the main features of the wave functions are key factors in determining the selection rules and the absorption intensity of the optical excitations. Similar gradient approximations have been successfully applied to investigate optical spectra of carbon-related systems, e.g., graphite [47], graphite intercalation compounds [51], carbon nanotubes [52], few-layer graphenes [53], and graphene nanoribbons [54].

3. Uniform magnetic field combined with a modulated magnetic field

Low-energy band structures of MG exhibit rich features in the presence of magnetic fields. The uniform perpendicular magnetic field causes the states to congregate and induces dispersionless Landau levels (LLs), indicated by the red curves in Fig. 2 for $B_0 = 4$ T. The unoccupied LLs and occupied LLs are symmetric about the Fermi level ($E_F = 0$). Each LL is characterized by the quantum number $n^{c,v}$, which corresponds to the number of zeros in the eigenvectors of harmonic oscillators [42, 55]. Each LL is fourfold degenerate for each (k_x, k_y) state without considering the spin degeneracy. Its energy can be approximated by a simple square-root relationship $|E_n^{c,v}| \propto \sqrt{n^{c,v} B_0}$ [8, 56], which is valid only for $|E_n^{c,v}| \leq 1$ eV [8].

The main characteristics of the LLs are affected by the modulated magnetic field, as shown in Fig. 2(a) by the black curves for $B_M = 0.5$ T and $R_M = 500$. Only the $n^{c,v} = 0$ LL remains unchanged, i.e., it retains its fourfold degeneracy at $E_F = 0$. On the other hand, each dispersionless LL with $n^{c,v} \geq 1$ splits into two periodic oscillation subbands with double degeneracy. The subbands possess two kinds of band-edge states, k_{be}^α and k_{be}^β , which are associated with the minimum field strength $B_0 - B_M$ and the maximum field strength $B_0 + B_M$, respectively. At a small modulation strength ($B_M/B_0 \leq 1/8$), the subbands oscillate between two LLs at the field strengths $B_0 \pm B_M$, as shown by the blue dashed lines in Fig. 2(a). The minimum and maximum of the oscillation subbands are proportional to $\sqrt{B_0 - B_M}$ and $\sqrt{B_0 + B_M}$, respectively. The surrounding electronic states at k_{be}^β congregate more easily, which results in a smaller band

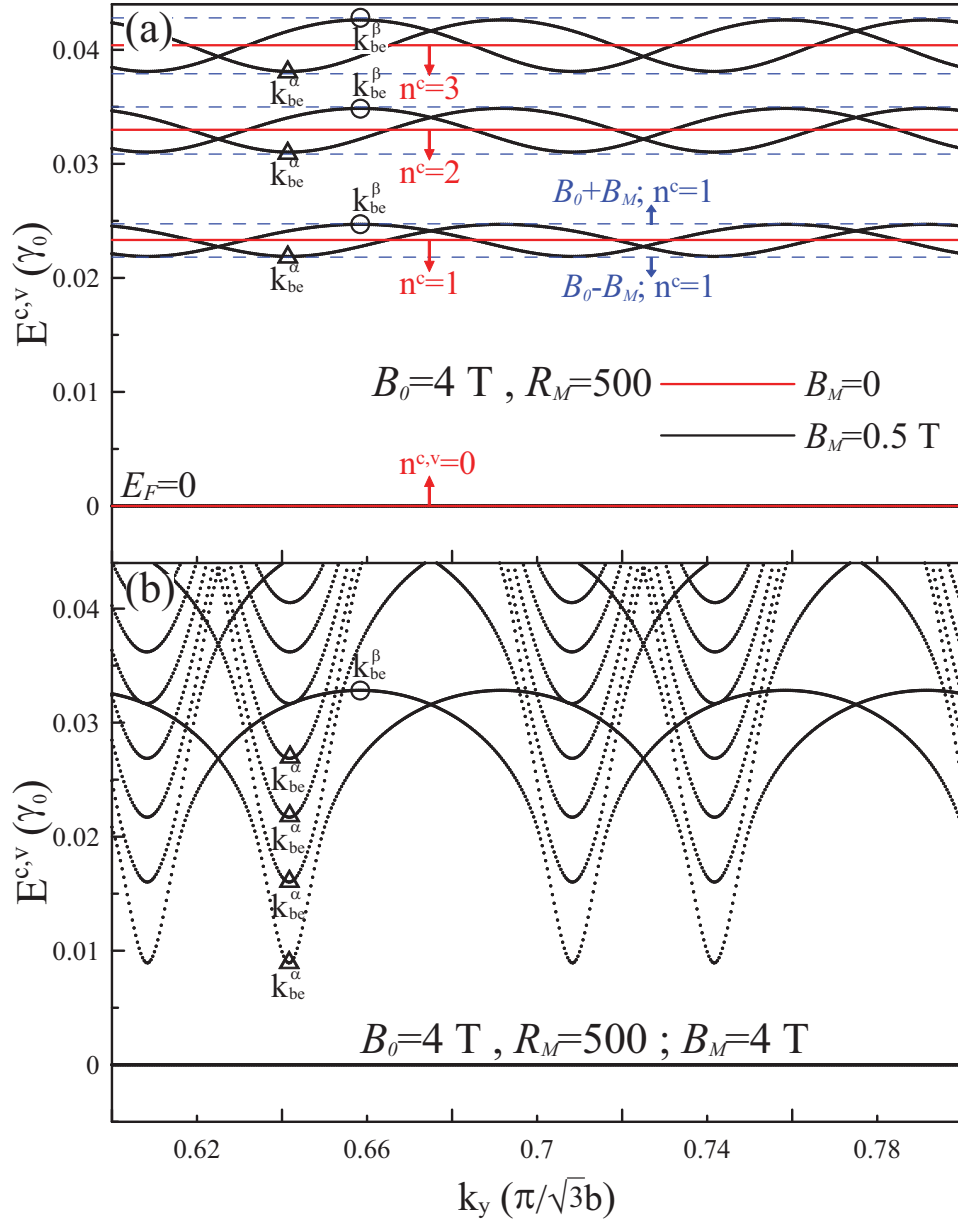


Fig. 2. The low k_y -dependent energy bands for $B_M \leq B_0$ case under (a) the uniform magnetic field $B_0 = 4$ T (red curves) and the composite field $B_0 = 4$ T in conjunction with $R_M = 500$ and $B_M = 0.5$ T (black curves), and (b) $B_0 = 4$ T in conjunction with $R_M = 500$ and $B_M = 4$ T. The triangular and circular symbols correspond to the band-edge states k_{be}^α and k_{be}^β , respectively.

curvature with a larger density of states (DOS). On the contrary, fewer states congregate at k_{be}^α , a situation leading to the larger band curvature and a smaller DOS.

The band structure may be considerably modified by increasing the strength of the modulated magnetic field. As B_M increases to the magnitude of B_0 , more complex energy spectra are introduced, as shown in Fig. 2(b) for $R_M = 500$ and $B_M = 4$ T. The oscillation subbands with $n^{c,v} \geq 1$ display wider oscillation amplitudes, stronger energy dispersions, and greater band curvatures. The strong oscillatory subbands with different quantum numbers overlap with one another, and the subband amplitudes are almost linearly magnified by B_M . The wave vectors associated with the band-edge states have no dependence on B_M . The greatest and smallest band curvatures occur at the local minimum k_{be}^α and the local maximum k_{be}^β , respectively. This implies that there are more k_{be}^α and fewer k_{be}^β in the lower state energies. However, a simple relation between the subband amplitudes and $\sqrt{B_0 \pm B_M}$ is absent.

An increase in the strength of the modulated field, as $B_M \gg B_0$, can drastically change the band structure. Figure 3(a) illustrates the complex oscillatory subbands for $R_M = 500$ and $B_M = 32$ T. The oscillation amplitudes do not demonstrate a simple relationship with B_M . It should be noted that neither the minima of the conduction bands nor the maxima of the valence bands exceed $E_F = 0$. Thus, there is no overlap between the conduction and valence bands, regardless of the modulation strength. The wave vectors of the band-edge states in the case of a large modulation strength ($B_M/B_0 \geq 8$) are different from those in the case of $B_M \leq B_0$ (depicted in Fig. 2). Therefore, each type of band-edge state corresponds to two different energies. The band-edge states belonging to the α (β) type own the two energies $k_{be}^{\alpha-}$ and $k_{be}^{\alpha+}$ ($k_{be}^{\beta-}$ and $k_{be}^{\beta+}$), as indicated by the orange and green triangles (blue and red circles) in the figure. Furthermore, the band structure in the composite fields displays band-edge state energies similar to those found under the influence of only a modulated magnetic field. In the presence of a pure modulated magnetic field, energy bands are partial flat bands at $E_F = 0$ and parabolic bands elsewhere, as shown in Fig. 3(b). Each parabolic subband has one specific band-edge state k_{be}^{sp} at $k_y = 2/3$ and four extra band-edge states k_{be}^{e+} 's and k_{be}^{e-} 's at both sides of $k_y = 2/3$ (indicated by the open circle and triangles), respectively. For the former, the energy of k_{be}^{sp} for the modulation strengths $B_0 + B_M$ and $B_0 - B_M$ is similar to those of $k_{be}^{\beta+}$ and $k_{be}^{\beta-}$, respectively. The latter k_{be}^{e+} and k_{be}^{e-} for the modulation strength B_M own the same energy as $k_{be}^{\alpha+}$ and $k_{be}^{\alpha-}$, respectively. The quantum number $n^{c,v}$ corresponding to the partial flat bands at $E_F = 0$ is defined as zero, and $n^{c,v} \geq 1$ are associated with the n -th ($n = 1, 2, 3 \dots$) conduction and valence parabolic subbands. The definition of $n^{c,v}$ is discussed in the following paragraph and graphically illustrated in Fig. 5.

The above-mentioned features of band structures influenced by the modulated magnetic fields would be reflected in the density of states (DOS). In the presence of a uniform magnetic field, DOS exhibits many delta-function-like peaks resulting from LLs, as shown by the red curve for $B_0 = 4$ T in Fig. 4(a). Such peaks suggest that LLs possess 0D energy levels. With an applied modulated magnetic field, each peak, except for the $n^{c,v} = 0$ LL at $E_F = 0$, splits into a pair of square-root divergent peaks ω_α and ω_β , as shown by the black curve in Fig. 4(a) for $R_M = 500$ and $B_M = 0.5$ T. The square-root divergence implies that the 0D energy level becomes the 1D energy band. Each pair of peaks ω_α and ω_β corresponds to the k_{be}^α and k_{be}^β states, respectively, and the peak frequencies are identical to those of LLs at $B_0 + B_M$ and $B_0 - B_M$. However, the two peaks ω_α and ω_β possess different peak heights owing to the distinct band curvatures at the two kinds of band edge states. The frequency and intensity are strongly dependent on the modulation strength. The peak heights decline and the spacing between ω_α and ω_β rises for a large modulation strength $B_M = 4$ T, as shown in Fig. 4(b). This reflects the fact that the greater curvatures and wider amplitudes of the oscillation subbands are a result of the

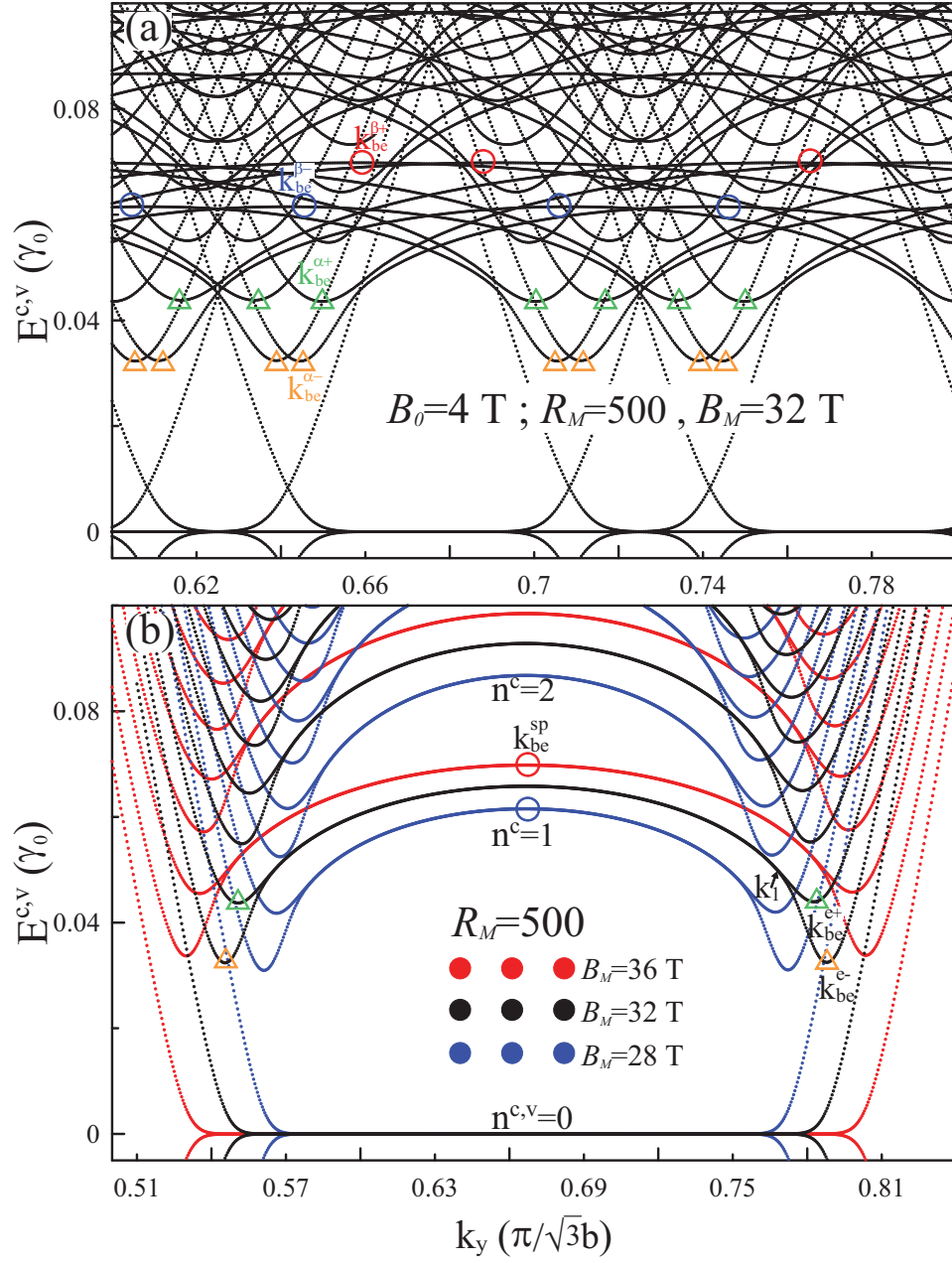


Fig. 3. The low k_y -dependent energy bands for the $B_M > B_0$ case at (a) the composite field $B_0 = 4$ T in conjunction with $R_M = 500$ and $B_M = 32$ T, and (b) the pure modulated magnetic field $R_M = 500$, $B_M = 36$, 32 and 28 T (red, black and blue curves, respectively). The triangular and circular symbols represent the same meanings as in Fig.2.

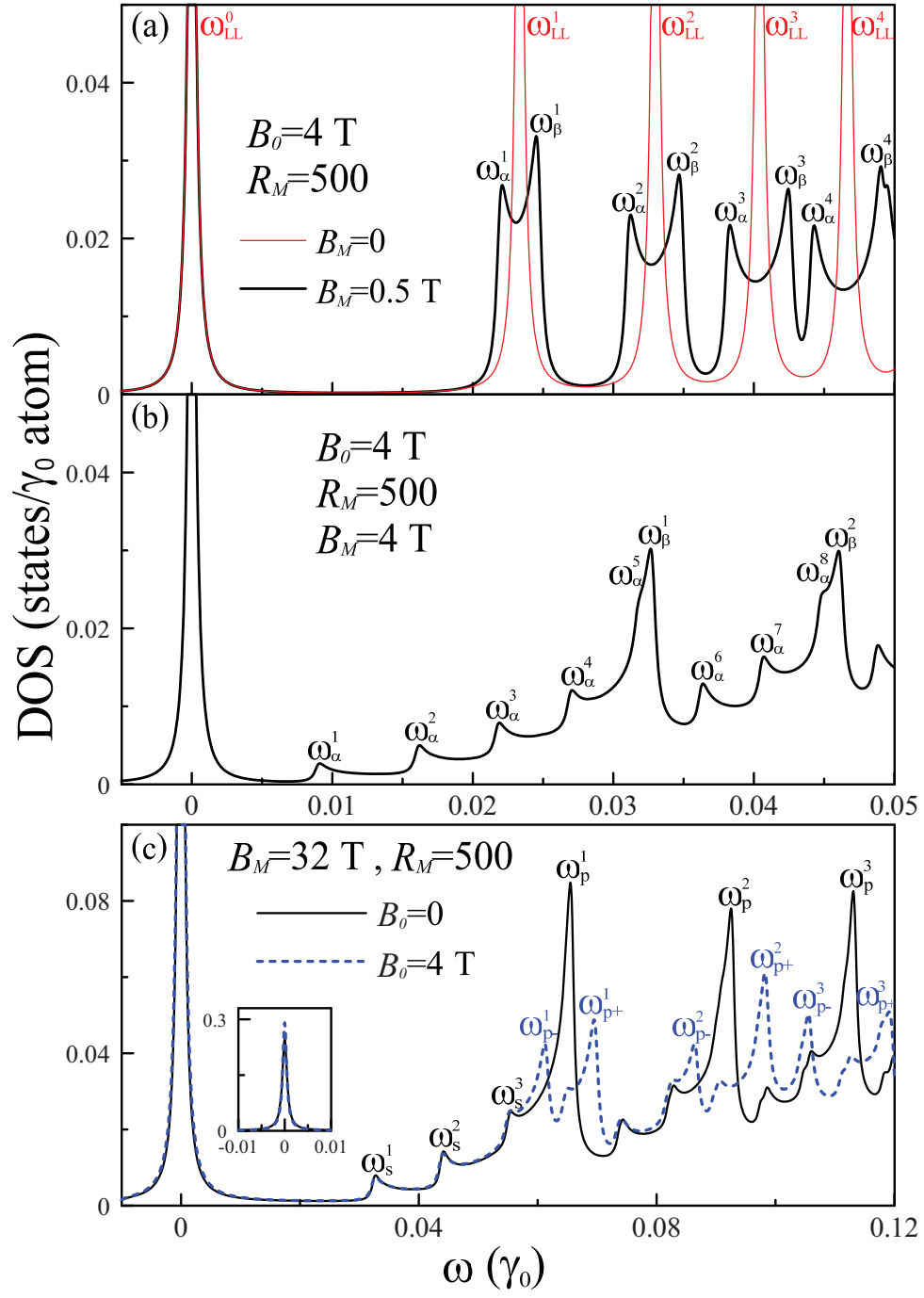


Fig. 4. The low-frequency density of states at (a) the uniform magnetic field $B_0 = 4$ T (red curves) and the composite field $B_0 = 4$ T in conjunction with $R_M = 500$ and $B_M = 0.5$ T (black curves), (b) $B_0 = 4$ T in conjunction with $R_M = 500$ and $B_M = 4$ T, and (c) $B_0 = 4$ T in conjunction with $R_M = 500$ and $B_M = 32$ T (blue curves), and the pure modulated magnetic field $R_M = 500$ and $B_M = 32$ T (black curves).

increasing B_M .

As the modulated field strength is further raised to $B_M = 32$ T (blue dashed curves in Fig. 4(c)), the DOS displays some features similar to those of the DOS in the modulated magnetic field where $R_M = 500$ and $B_M = 32$ T (black solid curves). The modulated magnetic field alone leads to a symmetric delta-function-like peak at $\omega = 0$ (inset in Fig. 4(c)), as well as asymmetric square-root divergent peaks. The former comes from the partial flat bands at $E_F = 0$. The latter can be further divided into weak subpeaks (ω_s^n) and strong principal peaks (ω_p^n) that are, respectively, dominated by the extra band-edge states (k_{be}^{e+} and k_{be}^{e-}) and specific band-edge states (k_{be}^{sp}). In the cases of a composite magnetic field, the frequencies and intensities of the subpeaks are almost the same as those in the modulated magnetic field alone. However, the principal peaks possess pair structures of ω_{p+}^n and ω_{p-}^n , which respectively correspond to the two different band-edge states $k_{be}^{\beta+}$ and $k_{be}^{\beta-}$.

The LL wave functions exhibit a specific spatial symmetry. Associated with the odd and even atoms, the wave functions in Eq. 1 have only a phase difference of π , that is, $A_{\mathbf{0}}^{c,v} = -A_{\mathbf{e}}^{c,v}$ and $B_{\mathbf{0}}^{c,v} = -B_{\mathbf{e}}^{c,v}$. Therefore, discussing only the amplitudes $A_{\mathbf{0}}^{c,v}$ and $B_{\mathbf{0}}^{c,v}$ is sufficient for understanding the main characteristics of the LLs. The LL wave functions, which is the eigenvector of the simple harmonic oscillation, can be described by an $n^{c,v}$ -th order Hermite polynomial multiplied by a Gaussian function, as shown in Fig. 5. These wave functions are distributed around the localization center, that is, at the $5/6$ position of the enlarged unit cell. Similar localization centers corresponding to the other degenerate states occur at the $1/6$, $2/6$, and $4/6$ positions. However, it is adequate to only consider any one center in evaluating the absorption spectra due to their identical optical responses. A simple relationship exists between the two sublattices of a - and b -atoms, i.e., $A_{\mathbf{0}}^{c,v}$ of $n^{c,v}$ is linearly proportional to $B_{\mathbf{0}}^{c,v}$ of $n^{c,v} + 1$. Moreover, the conduction and valence wave functions are related to each other by $A_{\mathbf{0}}^c = A_{\mathbf{0}}^v$ and $B_{\mathbf{0}}^c = -B_{\mathbf{0}}^v$.

The modulated field has strong effects on the LL wave functions, but plays no role in the relationship between the valence and conduction states. The wave functions corresponding to k_{be}^{α} , labeled in Fig. 3(a), are located at the minimum field strength $B_0 - B_M$. They exhibit slightly broadened and reduced amplitudes, as indicated by the black curves in Figs. 5(a)-5(d) for a small $B_M = 0.5$ T. However, the spatial symmetry of the wave functions remains unchanged. The simple relationship between $A_{\mathbf{0}}^{c,v}$ and $B_{\mathbf{0}}^{c,v}$ of the wave functions is almost preserved. A stronger modulation strength results in greater spatial changes of the wave functions, as shown in Figs. 5(e)-(f) for $B_0 = B_M = 4$ T. An increased broadening and asymmetry of the spatial distributions at $n^{c,v} = 0$ are revealed. On the other hand, spatial distributions with $n^{c,v} \geq 1$ are only widened (i.e., $n^c = 1$ in Figs. 5(g) and 5(h)), whereas their spatial symmetry is retained.

With a large modulation strength $B_M \gg B_0$, the wave function is characterized by a narrow distribution and an increased amplitude, as shown in Figs. 5(i)-5(l). For $n^{c,v} = 0$, the symmetry of the wave functions is almost restored. The amplitude $B_{\mathbf{0}}^{c,v}$, owing to the fact that it has the same number of zeros as $A_{\mathbf{0}}^{c,v}$, also contributes to the wave function. This means that carrier transfers occur between the a - and b -atoms. For $n^{c,v} \geq 1$, the spatial symmetry is broken and the zero mode is changed. The wave functions at $k_{be}^{\alpha+}$ and $k_{be}^{\alpha-}$ are different combinations of two subenvelope functions, of which the location centers are at zero net field strength, as indicated by the green and orange curves, respectively. These features are also obtained in the pure modulated magnetic field case. The wave functions associated with $k_y = k_1$ for $B_M = 32$ T and $R_M = 500$ in Fig. 4(b) have two nearly overlapping subenvelope functions ϕ_1 and ϕ_0 with respect to 1 and 0 zero points, as shown in Figs. 5(m)-5(p) by the green and orange dashed curves. The quantum number $n^{c,v}$ is defined by the larger number of zeros of the subenvelope functions. As the wave vector moves toward the extra band-edge states k_{be}^{e+} and k_{be}^{e-} , the two subenvelope functions ϕ_1 and ϕ_0 shift to the center located at zero net field strength and overlap

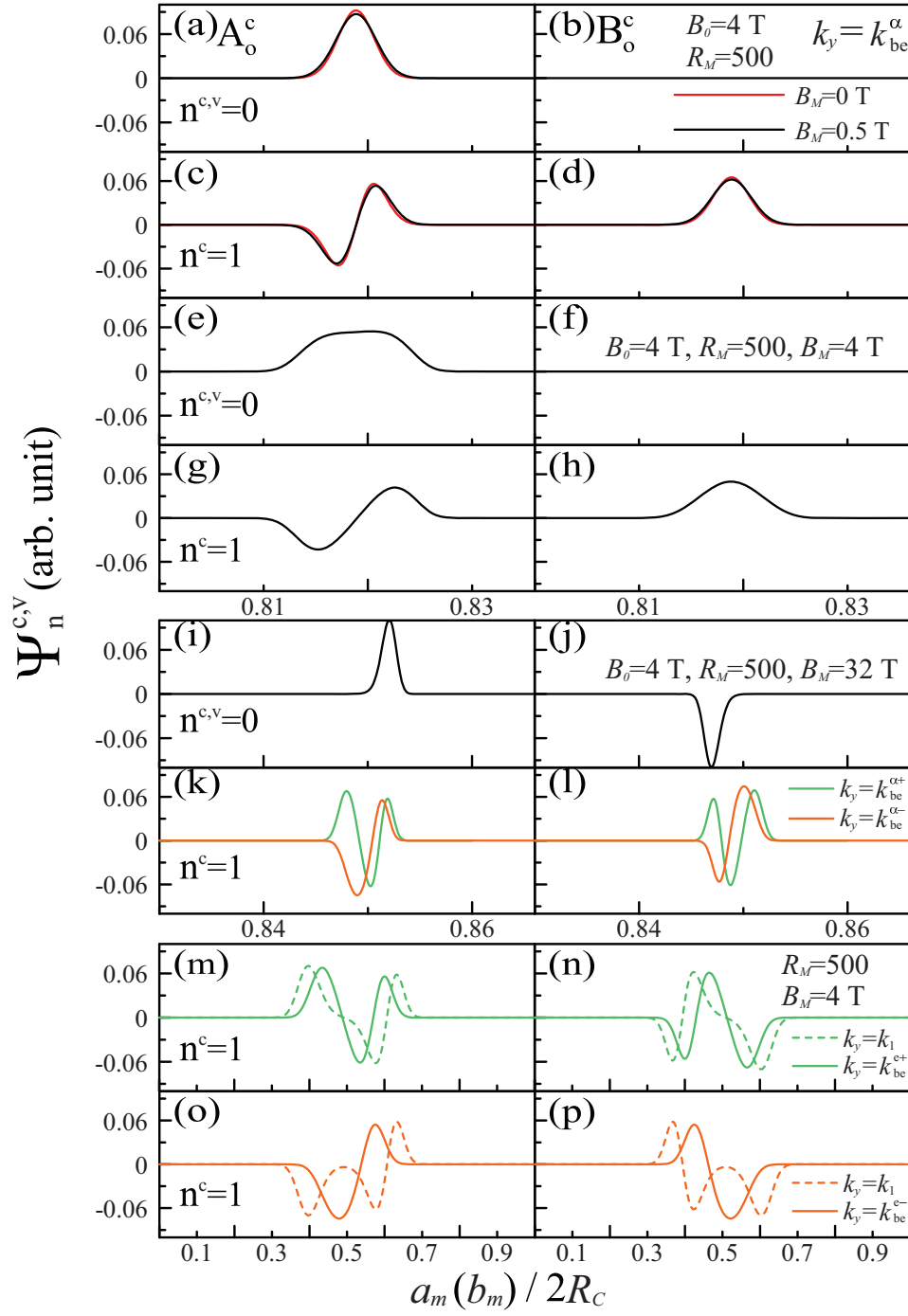


Fig. 5. The wave functions with $n^{c,v} = 0$ and $n^c = 1$ at k_{be}^α for (a)-(d) the uniform magnetic field $B_0 = 4$ T (red curves) and the composite field $B_0 = 4$ T together with $R_M = 500$ and $B_M = 0.5$ T (black curves), (e)-(h) $B_0 = 4$ T combined with $R_M = 500$ and $B_M = 4$ T, and (i)-(l) $B_0 = 4$ T combined with $R_M = 500$ and $B_M = 32$ T. The wave functions with $n^c = 1$ at k_1 (solid curves) and $k_{be}^{e\pm}$ (dashed curves) in the pure modulated field $R_M = 500$ and $B_M = 32$ T, are shown in (m)-(p).

with each other. For example, the overlapping wave functions A_0^c correspond to k_{be}^{e+} and k_{be}^{e-} superpositioned by the different combinations of $\phi_0 + \phi_1$ and $-\phi_0 + \phi_1$, indicated by the green and red curves, respectively.

The low-frequency optical absorption spectrum of the LLs presents numerous features. Many delta-function-like peaks with an identical intensity exist, as shown in Fig. 6(a) for $B_0 = 4$ T by the red curves. A single peak $\omega_{LL}^{nn'}$ comes from two equivalent transition channels: from the valence LL of n^v (n^v) to the conduction LL of n^c (n'^c). The quantum numbers related to the transition between the LLs must obey the specific selection rule $\Delta n = |n'^c(v) - n^{v(c)}| = 1$. The main reason for this is that the velocity matrix M^{cv} has a non-zero value only when $A_0^{c,v}$ and $B_0^{c,v}$ possess the same number of zeros and it is a dominant factor for the optical excitations of the prominent peaks. However, the modulated magnetic field modifies the number and intensities of the absorption peaks. The delta-function-like peak splits into two kinds of square-root-divergent peaks $\omega_\alpha^{nn'}$ and $\omega_\beta^{nn'}$ with lower intensities, as shown by the black curves. The divergences of the former and the latter occur near the right- and left-hand sides of $\omega_{LL}^{nn'}$. Each $\omega_\alpha^{nn'}$ ($\omega_\beta^{nn'}$) originates from the transitions of $k_{be}^\alpha(n^v) \rightarrow k_{be}^\alpha(n^c + 1)$ and $k_{be}^\alpha(n^v + 1) \rightarrow k_{be}^\alpha(n^c)$ [$k_{be}^\beta(n^v) \rightarrow k_{be}^\beta(n^c + 1)$ and $k_{be}^\beta(n^v + 1) \rightarrow k_{be}^\beta(n^c)$], its absorption frequency is same as that generated from the LLs at $B_0 - B_M = 3.5$ T ($B_0 + B_M = 4.5$ T). This leads to a redshift for the threshold absorption frequency. The peak intensity of $\omega_\alpha^{nn'}$ is lower than that of $\omega_\beta^{nn'}$ since the DOS of k_{be}^α is weaker than that of k_{be}^β . These absorption peaks obey the selection rule $\Delta n = 1$, similarly to uniform magnetic field case. This is due to the fact that the simple relation between $A_0^{c,v}$ and $B_0^{c,v}$ of the wave functions is almost preserved, even though the modulated field does have some effects on the wave functions.

As the modulated field strength B_M is increased to $B_0 = 4$ T, the frequency, intensity, peak number and selection rules in the optical absorption spectrum have evident variety, as shown in Fig. 6(b). The frequencies of $\omega_\alpha^{nn'}$'s are largely reduced, but the opposite is true for $\omega_\beta^{nn'}$'s. The fact that the α and β band-edge states, respectively, approach or depart from $E_F = 0$ is the main reason. This might lead to an abnormal relationship of absorption frequencies in that $\omega_\alpha^{nn'}$'s with the large $n^{c,v}$'s occur at a lower frequency than $\omega_\beta^{nn'}$ with the small $n^{c,v}$'s. For example, ω_α^{12} , ω_α^{67} and ω_α^{910} are smaller than ω_β^{01} , ω_β^{12} and ω_β^{23} , respectively. The ratio between the intensities of $\omega_\alpha^{nn'}$ and $\omega_\beta^{nn'}$ is further diminished with increasing B_M . This can be clearly observed in transitions with small $n^{c,v}$'s, i.e., ω_β^{01} is ten times stronger than ω_α^{01} in terms of the intensity. Moreover, more absorption peaks exist when B_M is increased. In addition to the peaks $\omega_\alpha^{nn'}$ and $\omega_\beta^{nn'}$ obeying the selection rule $\Delta n = 1$, two extra peaks with $\Delta n = 2$ and 3, ω_α^{02} and ω_α^{03} , are generated. These two peaks reflect the fact that the wave functions of the LLs with $n^{c,v} = 0$ are drastically changed by the modulated magnetic field.

As the modulated field strength is further raised to $B_M = 32$ T (red dashed curves in Fig. 7), the absorption spectrum displays certain important features in the pure modulated magnetic field where $R_M = 500$ and $B_M = 32$ T (black solid curves in Fig. 7). When the absorption peaks are dominated by the modulated magnetic field, they can be divided into principal peaks ω_p^{nn+1} and subpeaks $\omega_s^{nn'}$. These two kinds of peaks are not only seen in the modulated magnetic field case, but also appear in the composite magnetic field case as $B_M \gg B_0$. The subpeaks $\omega_s^{nn'}$ with the left-hand divergence arise from transitions between α type band-edge states (extra band-edge states) with the quantum number n and n' in the $B_M \gg B_0$ case (only B_M case). The association with the positions at zero net field strength are almost identical in both cases. However, we obtain two selection rules, $\Delta n = 0$ and $\Delta n = 1$, due to the complex overlapping behavior of two subenvelope functions in the wave function. On the other hand, the princi-

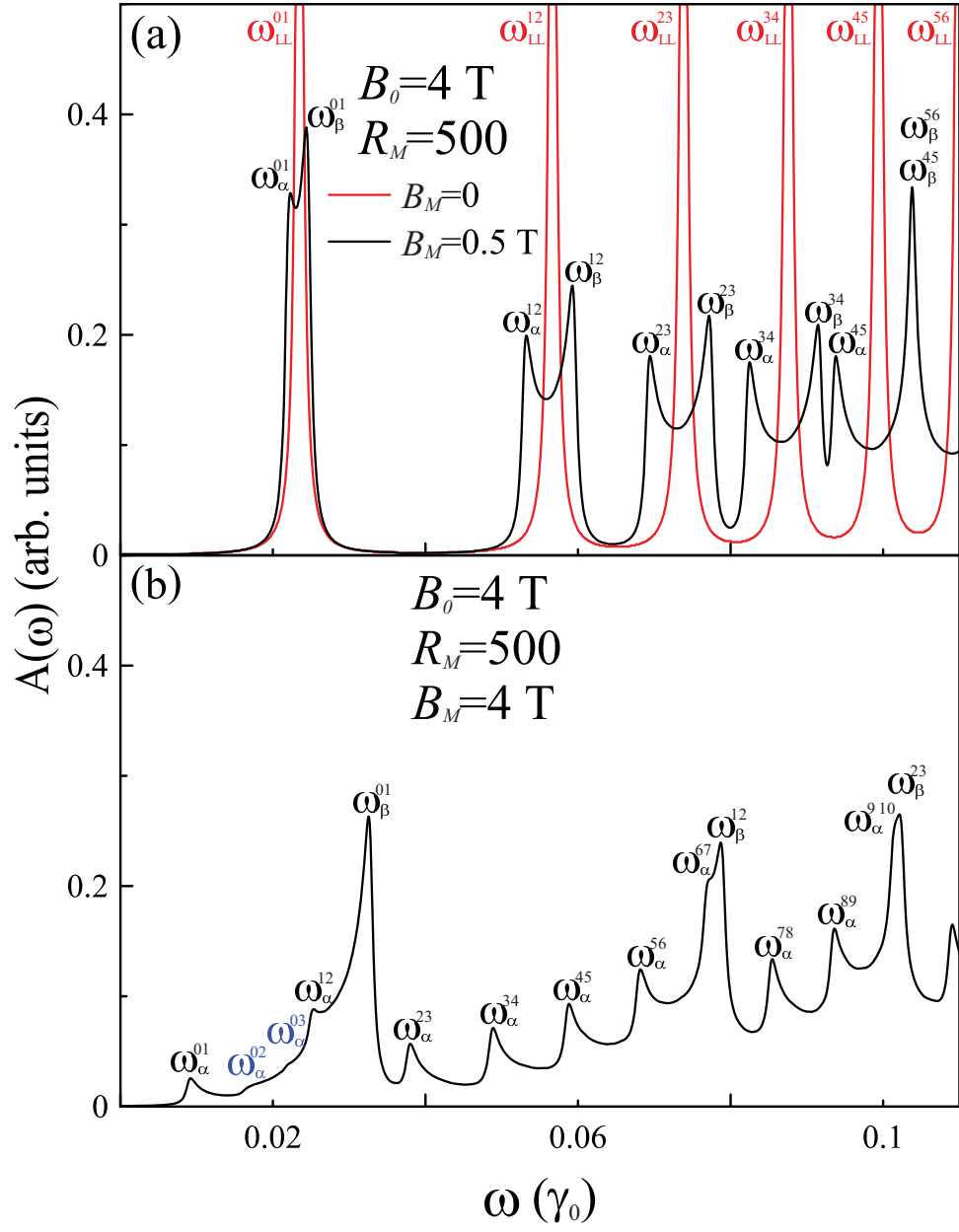


Fig. 6. The low-frequency optical absorption spectra for the $B_M \leq B_0$ case corresponding to (a) the uniform magnetic field $B_0 = 4$ T (red curve) and the composite field $B_0 = 4$ T together with $R_M = 500$ and $B_M = 0.5$ T (black curve) and (b) the composite field $B_0 = 4$ T combined with $R_M = 500$ and $B_M = 4$ T.

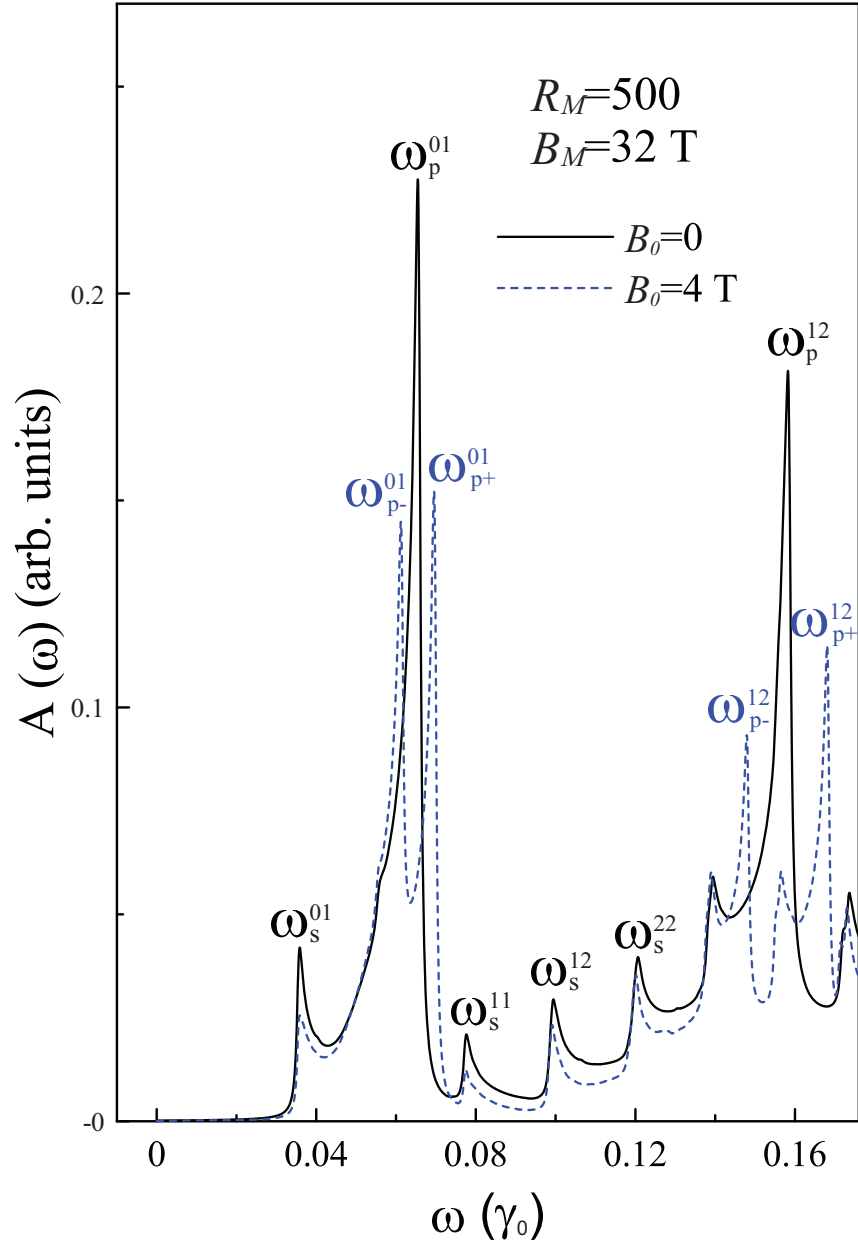


Fig. 7. The low-frequency optical absorption spectra for the $B_M > B_0$ case corresponding to the composite field $B_0 = 4 \text{ T}$ combined with $R_M = 500$ and $B_M = 32 \text{ T}$ (dashed blue curve) and the pure modulated magnetic field $R_M = 500$ and $B_M = 32 \text{ T}$ (black curve).

pal peaks ω_p^{nn+1} with right-hand divergence are much stronger than the subpeaks. They are attributed to the higher DOS consisting of the β type edge-states (specific band-edge states) with the quantum numbers n and $n+1$ in the composite field $B_M \gg B_0$ (pure modulated field). These absorption peaks obey the selection rule $\Delta n = 1$, similarly to the uniform magnetic field case. The principal peaks, however, possess a pair of peaks with ω_{p-}^{nn+1} and ω_{p+}^{nn+1} , which respectively correspond to two different field strengths, $|B_0 - B_M| = 28$ T and $|B_0 + B_M| = 36$ T, and thus the difference between the two field strengths leads to distinct absorption frequencies. For $B_M \gg B_0$, one can anticipate that the frequency discrepancy between the pair ω_{p-}^{nn+1} and ω_{p+}^{nn+1} becomes very small and eventually merges into a single peak, ω_p^{nn+1} , i.e., the absorption spectrum is restored to the status of the pure modulated magnetic field case.

The absorption frequency dependence on the modulated field strength is shown in Fig. 8 for $R_M = 500$ and $B_0 = 4$ T. In the range $B_M \leq B_0$, the absorption peaks can be further divided into two categories based on the different field dependence. The frequencies of $\omega_{\alpha}^{nn'}$ grow with increasing field strength, while the frequencies of $\omega_{\beta}^{nn'}$ decline. Each of the absorption peaks $\omega_{\alpha}^{nn'}$ and $\omega_{\beta}^{nn'}$ has a linear relationship with B_M . This reflects the fact that the subband amplitudes are proportional to B_M within the range. It should be noted that the abnormal relationship of the absorption frequency, the intersection of $\omega_{\alpha}^{nn'}$'s with large $n^{c,v}$'s and $\omega_{\beta}^{nn'}$'s with small $n^{c,v}$'s, occurs at a sufficiently large modulated field. However, in the higher absorption frequency region or for the field range $B_M > B_0$, the linear relationship is broken since the subband amplitudes are no longer linearly magnified by B_M .

In addition to the modulated magnetic field, the modulated electric potential also induces rich features in the magneto-absorption spectra. In both cases, the four-fold degenerate LLs, except the $n^{c,v} = 0$ LL for the modulated magnetic field case, change into periodic oscillation subbands with double-degeneracy. The energy dispersions become stronger for an increased modulated field strength. With regard to the wave functions, the symmetry breaking of the LL spatial distributions is enhanced as the modulation potential or the quantum number grows. However, the asymmetry of the LL wave functions only at $n^{c,v} = 0$ is revealed when B_M is comparable to B_0 . This implies that the optical absorption spectrum simultaneously exhibits the original peaks of $\Delta n = 1$ and the extra peaks of $\Delta n \neq 1$. In the case of the modulated magnetic field, the extra selection rules, i.e., $\Delta n = 2$ and $\Delta n = 3$, come into existence only when B_M approximately equals B_0 . On the other hand, extra selection rules induced by the electric potential would be generated when the modulation strength is increased. The extra peaks of $\Delta n \neq 1$ are relatively easily observed at higher frequency.

4. Conclusion

The low-frequency optical absorption spectra in the presence of composite magnetic fields are studied by the generalized tight-binding model and gradient approximation. By means of controlling the ratio between B_M and B_0 , systematic research on the magneto-optical spectra of MG can be thoroughly carried out. Under a uniform magnetic field, many delta-function-like peaks with uniform intensities exist in the optical spectrum. Each peak is generated from the LLs and satisfies the specific selection rule $\Delta n = 1$. At $B_M \ll B_0$, each LL splits into two periodic oscillatory subbands with two kinds of band-edge states k_{be}^{α} and k_{be}^{β} , except for the LL with $n^{c,v} = 0$. Nevertheless, the spatial symmetry of the wave functions remains unchanged. The simple relationship between $A_0^{c,v}$ and $B_0^{c,v}$ of the wave functions is almost preserved. Optical spectra exhibit many pairs of square-root-divergent peaks $\omega_{\alpha}^{nn'}$ and $\omega_{\beta}^{nn'}$ that obey the selection rule $\Delta n = 1$. The two peak frequencies associated with k_{be}^{α} and k_{be}^{β} are the same as those generated from the LLs at $B_0 - B_M$ and $B_0 + B_M$, respectively. The implication is that a red-shift occurs in the threshold absorption frequency. When B_M is increased to the magnitude of

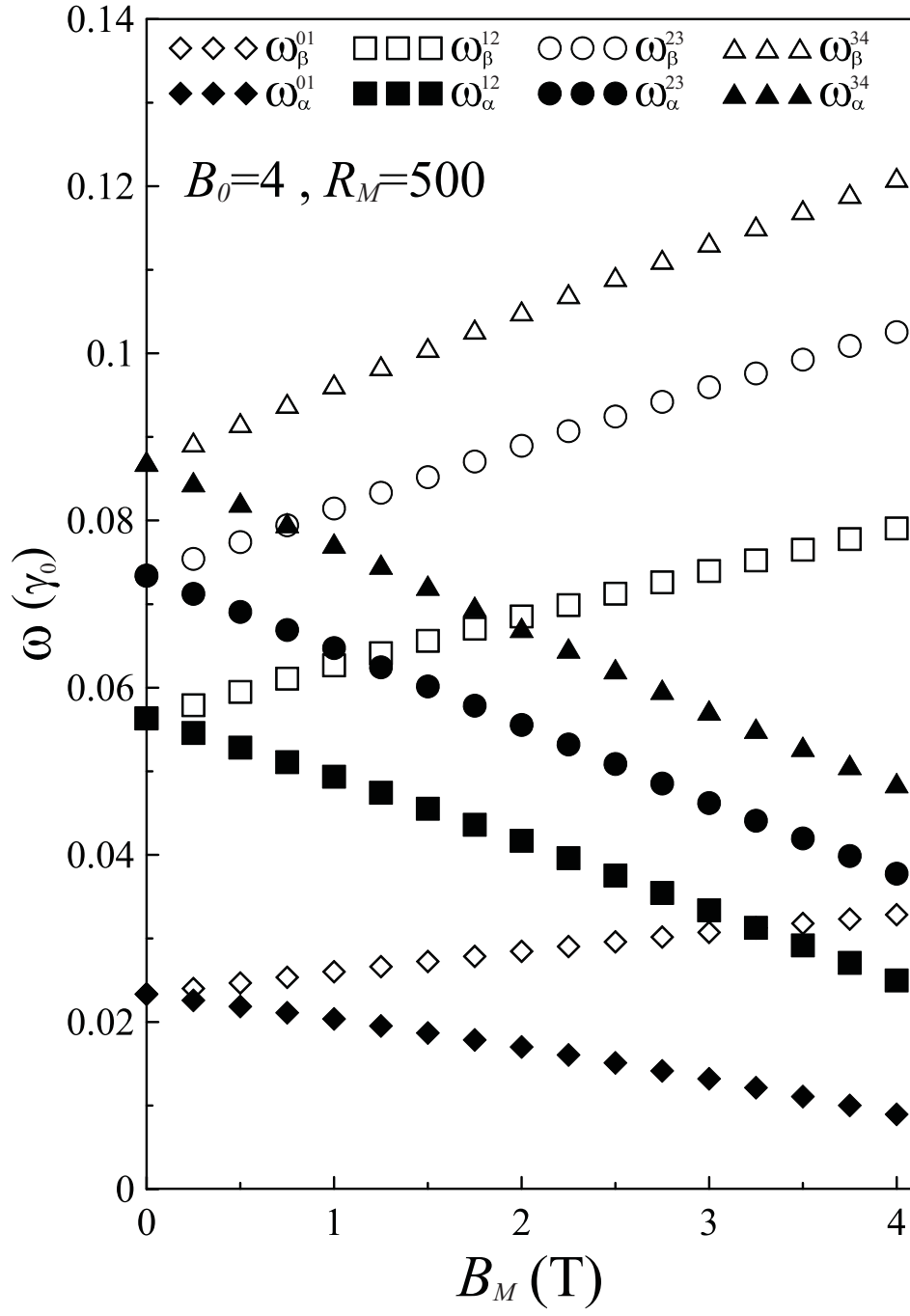


Fig. 8. The dependence of absorption frequencies $\omega_{\alpha}^{nn'}$ and $\omega_{\beta}^{nn'}$ with $|\Delta n| = |n - n'| = 1$ on the modulated strength B_M at $B_0 = 4$ T and $R_M = 500$.

B_0 , the oscillatory subbands display stronger energy dispersions and greater band curvatures. The strong oscillatory subbands with different quantum numbers overlap with one another. The wave functions exhibit broadened and reduced spatial distributions. In particular, the spatial symmetry of $n^{c,v} = 0$ is severely broken, which thus leads to the inclusion of extra peaks of $\Delta n \neq 1$ in the absorption spectrum. Moreover, an abnormal relationship of absorption frequencies exists in the optical spectra, i.e., $\omega_{\alpha}^{nn'}$'s with large $n^{c,v}$'s occur at frequencies lower than $\omega_{\beta}^{nn'}$ with small $n^{c,v}$'s. As the modulated field strength is raised to $B_M \gg B_0$, the optical spectra display certain features similar to those presented in the case of a pure modulated field B_M . Both cases contain the two selection rules $\Delta n = 0$ and $\Delta n = 1$, mainly owing to the complex overlapping behavior of two subenvelope functions in the wave function. However, in the case $B_M \gg B_0$, the principal peaks consist of a pair of peaks that respectively correspond to the two different field strengths $B_M \pm B_0$.

Very importantly, the generalized tight-binding model is developed to study monolayer graphene under various kinds of external fields. These fields can be uniform magnetic fields, modulated electric fields, modulated magnetic fields, and composite fields. The Hermitian Hamiltonian matrix used to determine the magneto-electronic properties becomes very large for the experimental field strengths. By means of rearranging the tight-binding functions, it is possible to transform this huge matrix into a band-like one to improve computational efficiency. The computation time can be further reduced by utilizing the characteristics of wave function distributions in the sublattices. In the generalized tight-binding model, the π -electronic structure of MG is exactly solved over the wide energy range ± 5 eV, a solution that has proven to be valid even if a magnetic, electric or composite field is applied. Although the important interlayer interactions are not used in this case, the developed method is a generalized treatment more than just perturbations. This model is not only suitable in theoretical calculations of MG, but can also be extended to other stacked layer systems, i.e., AA-, AB-, ABC-stacked [53, 55, 57-59] and bulk systems [60]. The present study should prove very useful for comprehending other physical properties, such as Coulomb excitations [61-66] and transport properties [67-71].

Acknowledgments

This work is supported by the NSC of Taiwan, under Grant No. NSC 102-2112-M-006-007-MY3.